Title	On DEM simulation of loose packing behaviour of fine and cohesive particles
Author(s)	Washino, Kimiaki; Chan, Ei L.; Faroux, Dorian et al.
Citation	Advanced Powder Technology. 2025, 36(3), p. 104809
Version Type	VoR
URL	https://hdl.handle.net/11094/101299
rights	This article is licensed under a Creative Commons Attribution 4.0 International License.
Note	

Original Research Paper

On DEM simulation of loose packing behaviour of fine and cohesive particles

Kimiaki Washino [a,b,*], Ei L. Chan [a,b], Dorian Faroux [a,b], Takuya Tsuji [a,b], Tatsuya Takahashi [c], Shuji Sasabe [c]

[a] Department of Mechanical Engineering, Osaka University, Suita, Osaka 565-0871, Japan
[b] DENSE Ltd., Osaka Kita-ku, Osaka 530-0001, Japan
[c] Hosokawa Micron Corporation, Hirakata, Osaka 573-1132, Japan

ABSTRACT

While Discrete Element Method (DEM) is widely used to simulate fine and cohesive granular materials, accurately capturing real-life packing behaviour requires further investigation on the (i) types of attraction forces and (ii) cluster formation during free fall. In the present study, simulations of various scenarios have been performed to investigate the impacts of particle insertion methods on the resultant packing fraction. The results suggest that the introduction of initial vertical velocity fluctuations during stream insertion can lead to consistent formation of clusters of free falling particles, which is a key factor for achieving loose packing of cohesive particles. We then tested and compared two commonly used attraction force models: the JKR surface adhesion force and non-bonded van der Waals force models. It is revealed that the packing fractions and coordination numbers of the final beds are comparable across different attraction force models as long as the following two conditions are met at the same time: (i) the surface energy density is adjusted (by approximately 2.6 times) to match the total potential energy between a pair of particles and (ii) the initial vertical velocity fluctuations are assigned to form particle clusters during free fall.

1. Introduction

Packing of granular materials is crucial in various industrial processes. Most evidently, it directly impacts the design and selection of packaging and storage equipment. Many unit operations such as mixing, tableting and screening start with gravitational filling of granular materials in containers. Moreover, bulk and tapped density measurements are often utilised to characterise the flowability and compactability. Therefore, the way granular materials pack has been a subject of study for many researchers [1–3].

Packing fraction is the simplest and most accessible macroscopic parameter for the characterisation of packed granular materials [4]. Granular materials are collections of microscopic particles, and the resultant packing fraction is influenced by the particle properties. The packing fraction of coarse particles (of the order of millimetres in size) can be higher than 0.6, whilst that of fine particles (of the order of micrometres) may only reach 0.2 or 0.3. This is because the inter-particle attraction forces (e.g., surface

adhesion and van der Waals forces) are more dominant than the gravitational force for fine particles [5], which leads to tree- or chain-like packing structure as well as cluster formation [6]. Several empirical and semi-empirical expressions are proposed in the literature to predict packing fraction [6,7], but it is still challenging to account for various particle properties.

Computer simulation can be a powerful tool to study the packing behaviour of granular materials, and one of the most widely used methods is Discrete Element Method (DEM) [8]. In DEM, the forces and torques exerted on individual particles are explicitly computed to solve the equations of motion. This makes it an ideal tool to study the impacts of microscopic particle properties (such as size [9], electrostatic charge [10], types of inter-particle attraction forces [11], polydispersity [12], shape [13], frictions [14]) and stiffness [15]) on packing fraction.

Majority of the DEM simulations of fine particles in the literature consider either one or both of the following two attraction forces: the surface adhesion force [16,17,12,18] and/or non-bonded van der Waals force [19,9,20,10,17,15]. The JKR theory [21] is often used to model the surface adhesion force as a function of the contact area between particles. On the other hand, the Hamaker theory [22] is usually employed for the non-bonded

* Corresponding author at: Department of Mechanical Engineering, Osaka University, Suita Osaka 565-0871, Japan.
  E-mail address: washino.k@mech.eng.osaka-u.ac.jp (K. Washino).

van der Waals force, which is non-zero even when the particles are apart from each other. Although both the JKR and non-bonded models can be related to the surface energy density [11], they are formulated in a completely different manner.

Parteli et al. [11] found in their simulations that it was necessary to consider non-bonded van der Waals force in DEM to obtain experimentally observed loose packing of fine particles. In their experiment with fine glass ballotini, the packing fraction steeply declined as the average particle size decreased below approximately 25 μm. Their simulations yielded a consistent trend when both the JKR and non-bonded models were incorporated, but using only the JKR model was proven insufficient as can be seen in Fig. 1. However, to the best of the authors' knowledge, the exact reason why the non-bonded force is necessary to achieve loose packing is not understood yet.

It is a relatively straightforward and standardised process to measure the packing fraction experimentally: particles of known (true) density are poured into a moderately sized cup (several centimetres in diameter and height), and their volume is determined from the measured mass to compute the packing fraction. However, simulating this process with fine particles using DEM is computationally challenging due to the enormous number of particles required to be tracked. Therefore, many simulations in the literature employ very small domain size (about 10 to 20 times the average particle diameter) with periodic boundary conditions. This may be sufficient for capturing the aforementioned tree- or chain-like structures but questionable for the inter-cluster structures.

For example, Fig. 2 shows Scanning Electron Microscope (SEM) images of basic aluminium sulphate powder (Taimei Chemicals, Japan), which are (a) collected from the surface of a natural heap and (b) dispersed to show the individual particles. The particles are almost cubic in shape with an approximate edge length of 3 μm (Fig. 2b), and experimentally measured packing fraction using PT-X (Hosokawa Micron, Japan) is 0.25. In Fig. 2a, the particles form clusters (indicated with red circles), i.e., regions where particles are relatively concentrated, and large voids (indicated with yellow circles) can be observed between them. The size of the both clusters and voids can be larger than 10 times the individual particle size, which may be difficult to be captured if the simulation domain is small as mentioned above. While previous studies have examined the cluster formation of free falling fine particles experimentally [23–26] and numerically [27–29], the effect of cluster formation to the resulting packing fraction remains unexplored in the literature.
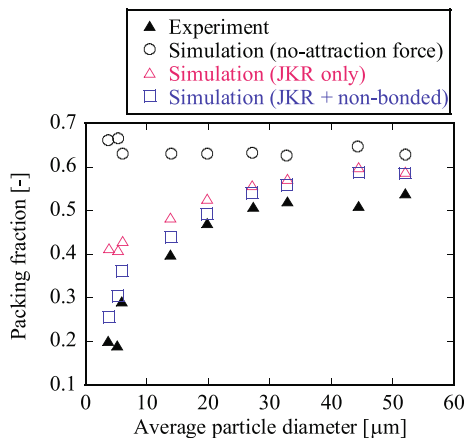
This study aims to fill the aforementioned knowledge gaps by numerically investigating the impacts of (i) type of attraction forces (i.e., surface adhesion force and non-bonded van der Waals force) and (ii) cluster formation during free fall on the packing behaviour of fine and cohesive particles using DEM. We compare different types of attraction forces in terms of the total potential energy between a pair of particles, which is related to the separation energy to pull-off a pair of particles from an equilibrium state [30,31]. Initial vertical velocity fluctuation is introduced and varied during particle generation to control the cluster formation. To simplify the analysis and focus on the primary objective, the effect of air resistance is not considered here. LIGGGHTS [32] is used as the simulation platform, which is open-source and fully customisable.

2. Theory

2.1. Discrete Element Method

The model for DEM simulation has been reported in the authors' previous work in detail [33,34], and the outline is briefly explained in this section. The governing equations of Particle i interacting with adjacent Particle j is given by:

$$m_i \dot{\boldsymbol{v}}_i = \sum_j \boldsymbol{F}_{IPij} + \boldsymbol{F}_{Bi} \tag{1}$$

$$\dot{\boldsymbol{L}}_i = \sum_j \boldsymbol{M}_{IPij} \tag{2}$$

$$\boldsymbol{L}_i = \boldsymbol{I}_i \boldsymbol{\omega}_i \tag{3}$$

where m is the particle mass, $\boldsymbol{v}$ is the translational velocity, $\boldsymbol{F}_{IP}$ is the inter-particle forces, $\boldsymbol{F}_B = m\boldsymbol{g}$ is the body (gravitational) force, $\boldsymbol{L}$ is the angular momentum, $\boldsymbol{M}_{IP}$ is the inter-particle torques, $\boldsymbol{I}$ is the tensor of inertia, and $\boldsymbol{\omega}$ is the angular velocity. The superquadric function is used to implicitly express the particle shape [35]:

$$f(\boldsymbol{X}) = \left(\left| \frac{X}{a} \right|^{n_2} + \left| \frac{Y}{b} \right|^{n_2} \right)^{n_1/n_2} + \left| \frac{Z}{c} \right|^{n_1} - 1 \tag{4}$$

$$\boldsymbol{X} = (X, Y, Z)^{\mathrm{T}} \tag{5}$$

where a, b, and c are the size parameters in each principal axis, and n_1 and n_2 are the blockiness parameters that control the edge sharpness. $\boldsymbol{X}$ is the position vector (in local reference frame) from the particle centre, and the particle surface is defined as $f(\boldsymbol{X}) = 0$. Details of the contact detection algorithm for the superquadric model are explained in [36].

2.2. The JKR model

The JKR model [21] is employed for the calculation of adhesive contact force, $\boldsymbol{F}_C$. The normal and tangential contact forces are given by:

$$\boldsymbol{F}_{Cn} = -\left(\frac{4E^*}{3r^*} a_c^3 - 4\sqrt{\pi\gamma E^* a_c^3} + \eta_n \boldsymbol{v}_{rel} \cdot \boldsymbol{n} \right) \boldsymbol{n} \tag{6}$$

$$\boldsymbol{F}_{Ct} = -\min[8G^* \sqrt{r^* \delta_n} \delta_t + \eta_t v_s, \ \mu_s F_N] \boldsymbol{t} \tag{7}$$

where a_c is the contact radius [11], r is the volume equivalent sphere radius [37], E is the Young's modulus, γ is the surface energy density, η is the viscous damping coefficient [38], $\boldsymbol{v}_{rel}$ is the relative velocity, $\boldsymbol{n}$ is the unit normal vector, G is the shear modulus, δ is the

Fig. 1. Packing fraction as a function of average particle size. Reproduced from the work by Parteli et al. [11].
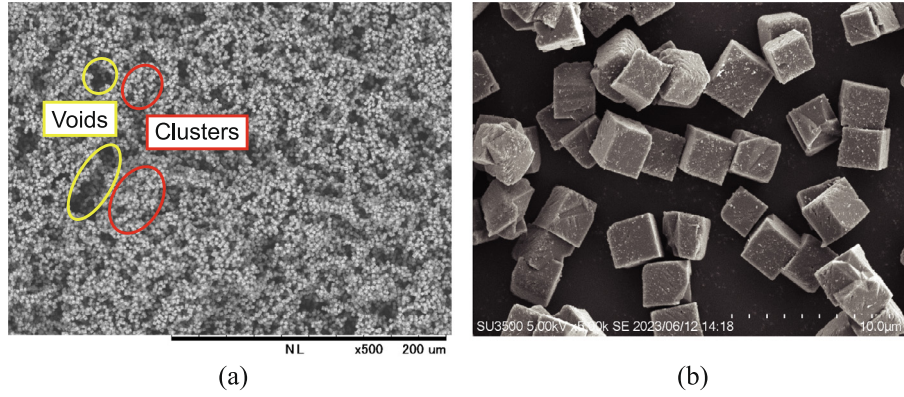
Fig. 2. SEM images of basic aluminium sulfate; (a) collected from the surface of a natural heap and (b) dispersed. Examples of clusters and voids are indicated with red and yellow circles, respectively.

particle deformation (overlap), v_s is the magnitude of the relative tangential velocity at the contact surface, μ_s is the coefficient of sliding friction, F_N is the normal load during sliding [39,40], and t is the unit tangent vector. The subscripts n and t indicate the normal and tangential directions, respectively, and the superscript * indicates the reduced quantities. Following many studies in the literature [41,11,30], the model is simplified so that the contact is broken as soon as the normal overlap becomes zero.

2.3. The non-bonded model

The non-bonded van der Waals force, $\boldsymbol{F}_{vdW}$, is given by [11]:

$$\boldsymbol{F}_{vdW} = \begin{cases} \frac{A_H r^*}{6D_{min}^2}\boldsymbol{n} & \text{if} \quad \delta_n \geqslant 0 \\ \frac{A_H r^*}{6(\delta_n - D_{min})^2}\boldsymbol{n} & \text{if} \quad -D_{max} \leqslant \delta_n < 0 \\ \boldsymbol{0} & \text{otherwise} \end{cases} \tag{8}$$

where A_H is the Hamaker constant, D_{min} is the minimum distance to avoid the singularity at $\delta_n = 0$ and D_{max} is the cut-off distance. Negative overlap ($\delta_n < 0$) means that the particle surfaces are not in contact. The Hamaker constant is given by:

$$A_H = 24\pi D_{min}^2\gamma \tag{9}$$

Strictly speaking, Eq. (8) is valid only for spherical particles. In general, accurate calculation of the non-bonded van der Waals forces for non-spherical particles requires numerical integration of intermolecular interactions [42,43], which can be computationally demanding. In this work, we focus on examining the influence of non-bonded forces to bulk particle packing, and Eq. (8) is employed as a simplified representation. This simplification is analogous to the use of volume equivalent sphere radius for the contact force calculation of non-spherical particles [37].

2.4. Treatment of inter-particle force and torque

When only adhesive contact force is considered, the inter-particle force becomes:

$$\boldsymbol{F}_{IP} = \boldsymbol{F}_C \tag{10}$$

We call this "JKR only model". When both adhesive contact and non-bonded van der Waals forces are taken into account, it goes:

$$\boldsymbol{F}_{IP} = \boldsymbol{F}_C + \boldsymbol{F}_{vdW} \tag{11}$$

This is referred to as "JKR + non-bonded model". Note that the non-bonded force is not included in F_N for the calculation of friction force. The inter-particle torques are computed by:

$$\boldsymbol{M}_{IP} = \boldsymbol{r} \times \boldsymbol{F}_{IP} \tag{12}$$

where $\boldsymbol{r}$ is the vector running from the centre of particle to the contact point (or the midway point of particle surfaces if the particles are not in contact).

2.5. Total potential energy between a pair of particles

The inter-particle forces in the normal direction (i.e., Eqs. (6) and (8)) are conservative except for the viscous damping force (the term containing η_n in Eq. (6)). Therefore, considering a quasi-static system, the total potential energy between two particles, U, can be defined as:

$$F_n = -\frac{\partial U}{\partial \delta_n} \tag{13}$$

$$U = U_{ER} + U_{SA} + U_{vdW} \tag{14}$$

where U_{ER} is due to the elastic repulsion force, U_{SA} is due to the surface adhesion force and U_{vdW} is due to the van der Waals force, which are associated with the first term of Eq. (6), the second term of Eq. (6) and Eq. (8), respectively. Fig. 3 is a schematic of the relationship between the total potential energy and overlap of two particles. The potential energy is zero when the particles are infinitely separated. The point where $-\partial U/\partial \delta_n = 0$ is an equilibrium point, and the depth of the well (indicated by the dashed arrow) is the separation energy required to pull-off the particles from the equi-
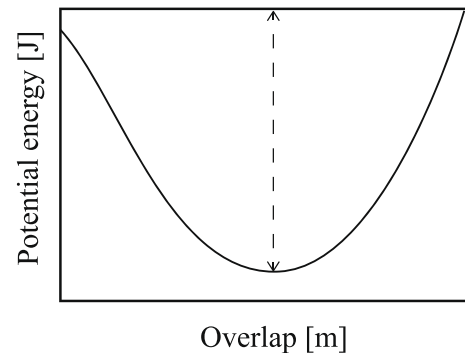

Fig. 3. Schematic of total potential energy between a pair of particles as a function of normal overlap.

librium state. While it is straightforward to obtain U_{vdW}, the theoretical expressions for U_{ER} and U_{SA} in the JKR model are more complicated. Therefore, the total potential energy is evaluated numerically in this work.

3. Particle properties

Table 1 shows common properties of the particles used in all simulations in this work. With the final goal of simulating the cubic particles shown in Fig. 2 in the future, we set the blockiness parameters ($n_1 = n_2$) to 8 and the size parameters ($a = b = c$) to 1.5 μm. This makes the edge length of the cube 3 μm with the volume equivalent sphere radius of 1.82 μm. A snapshot of the particle used is shown in Fig. 4. While the edges and corners are slightly rounded, the overall shape can be considered as a cube. Since particle rolling can be largely constrained by the particle shape, the rolling friction model is not used in this study. The values of D_{min} and D_{max} are from Parteli et al. [11].

The surface energy density is varied to change the cohesiveness of the particles. Two values of surface energy density are employed when considering the JKR + non-bonded model: 0.0004 and 0.004 J/m². In our preliminary tests, it is found that these (seemingly small) values are sufficient to make the particles cohesive. This is mainly due to the low Young's modulus used (5 MPa), which results in significant energy dissipation during prolonged particle contact. More details about the Young's modulus and cohesiveness of particles is discussed in the authors' previous work [44,45]. Fig. 5 shows the total potential energy defined in Eq. (14) using the properties in Table 1. We found that very similar potential energy curves can be obtained between the cases with the JKR only and JKR + non-bonded models if the surface energy density is appropriately adjusted: $\gamma = 0.00105$ and 0.0105 J/m² with the JKR only model are corresponding to $\gamma = 0.0004$ and 0.004 J/m² with the JKR + non-bonded model, respectively. They are called "equivalent surface energy density" in this work.

4. Results and discussion

4.1. At-once insertion of particles

In most, if not all, of the simulations studying the packing fraction of fine and cohesive particles in the literature, the particles are inserted using either of the following two methods. One is to randomly distribute particles over the entire simulation domain at the start of simulation [9,46,11,18]. The other is to feed particles sequentially and continuously from a near-top region of the simulation domain [47,48,12]. The former is called "at-once" insertion whilst the latter is referred to as "stream" insertion in this work. We present simulation results using the at-once insertion method in this section.

Table 1
Common properties of particles.

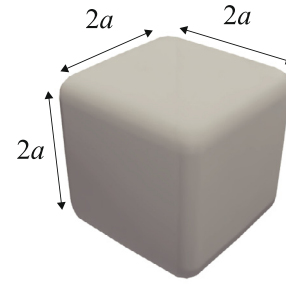| Property	Value
Size parameter $a = b = c$ [m]	1.5×10^{-6}
Blockiness parameter $n_1 = n_2$ [-]	8
Density [kg/m³]	2730
Young's modulus [Pa]	5×10^6
Poisson's ratio [-]	0.3
Coefficient of sliding friction [-]	0.5
Coefficient of restitution [-]	0.3
D_{min} [m]	1.65×10^{-10}
D_{max} [m]	1×10^{-6}

Fig. 4. Snapshot of the cubic particle used. The edge length is $2a = 3$ μm.

4.1.1. High initial packing fraction

First, we performed simulations in a similar manner as Parteli et al. [11] to reconfirm the impact of non-bonded forces. The simulation domain size is $(20 \times 2a) \times (20 \times 2a) \times (227 \times 2a)$ where $2a$ is the edge length of the cubic particle used. Periodic boundary conditions are applied in the horizontal directions, and flat plates are mounted at the top and bottom boundaries. The attraction forces between the top plate and particles are deactivated to avoid the particles adhering to the top wall. The same boundary conditions are employed in all simulations presented in this work. The particles are initially distributed randomly over the entire simulation domain with zero velocity and a packing fraction of 0.2 as shown in Fig. 6, and they settle under the influence of the gravity (9.81 m/s²). No overlap is permitted at the generation of the particles. The surface energy density used is 0.004 J/m². The particle generation method follows that of Parteli et al. [11], and the key simulation conditions are compared in Table 2. Although the particle properties differ, they are largely similar.

Fig. 7 shows the profiles of packing fraction of the final beds in the vertical direction from the bottom obtained from (a) JKR only model and (b) JKR + non-bonded model. The packing fraction is averaged over sub-domains of size $(20 \times 2a) \times (20 \times 2a) \times (2 \times 2a)$. The height of sub-domains is fixed to $(2 \times 2a)$ throughout the study. It can be seen that the variation with height is rather small except for the near-bottom region in Fig. 7b. The packing fraction of Fig. 7a is approximately 0.4 whilst that of Fig. 7b (excluding the near bottom region) is 0.21. In these simulations, the packing fraction does not reach a small value (below 0.4) with the JKR only model, while the non-bonded force has a significant impact as reported by Parteli et al. (Fig. 1).

Fig. 8 shows sequential snapshots of the particle beds where the particles are coloured based on the coordination number. The coordination number is defined as the number of particles whose bounding spheres, i.e., the minimal spheres that enclose the cubes, are in contact in this work. The particle colour changes from the bottom in Fig. 8a (JKR only model), indicating that a dense bed builds up from the bottom. The bed height decreases in a parabolic manner due to the continuous acceleration of the particles by gravity, and it becomes roughly half in the final state. In contrast, in Fig. 8b (JKR + non-bonded model), the colour of particles changes rather uniformly across the entire bed with time, and the difference of the bed height between the initial and final states is small. In both cases, no noticeable void can be observed.

4.1.2. Low initial packing fraction

In the next set of simulations, the domain height is extended to $(13333 \times 2a)$ and the initial packing fraction is reduced to 0.0034 as shown in Fig. 9, resulting in a much sparser particle distribution while keeping the same mass of particles. Fig. 10 shows the profiles of packing fraction of the final beds from the bottom. The packing
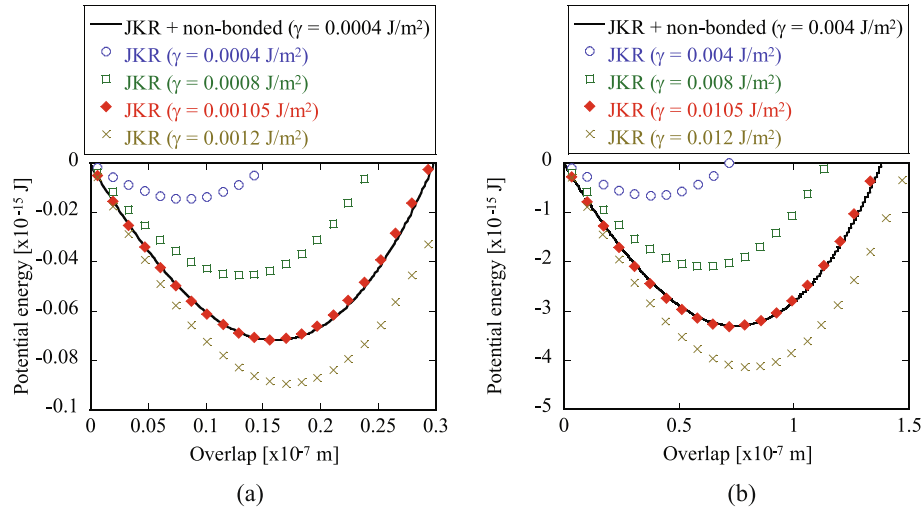
Fig. 5. Total potential energies as a function of the overlap with different surface energy densities; (a) intermediately cohesive and (b) highly cohesive cases.
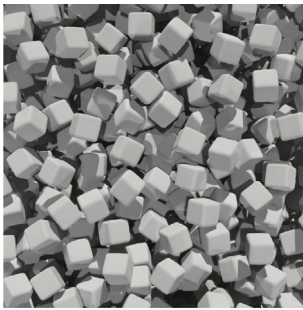

Fig. 6. Close-up view of particles generated with an initial packing fraction of 0.2, ensuring no particle overlap.

Table 2
Comparison between simulation conditions used in this work and Parteli et al. [11]. Note that $2a$ is the cube edge length and d_{ave} is the average sphere diameter.

	Present work	Parteli et al.
Particle shape	Cube	Sphere
Size distribution	Mono-dispersed	Poly-dispersed
Horizontal domain size	$20 \times 2a$	$20 \times d_{ave}$
Insertion method	At-once	At-once
Initial packing fraction	0.2	0.2
Initial particle overlap	None	None
Initial particle velocity	Zero	Zero

fraction profiles in Figs. 7a and 10a (JKR only model) are almost identical, but those in Figs. 7b and 10b (JKR + non-bonded model) are significantly different. Moreover, it can be observed that difference between the packing fractions near the bottom in Figures 10a and 10b is marginal.

Fig. 11 shows sequential snapshots of the particle beds. The particle beds with and without employing the non-bonded force for the first 40 ms looks more or less similar. After that, the particles start to form clusters in Fig. 11b, which are most prominent at 70 and 80 ms. This causes inhomogeneous coordination number distribution appearing as red patches, which leads to visible voids in the bed and smaller packing fraction.

The results in Figs. 7–11 offer the following insights. When only the JKR model is employed, particles interact with each other only when they are in contact. Since the particles do not overlap at the generation, the particles do not "feel" other particles during free fall. In other words, the particles are completely isolated regardless of the initial packing fraction until they land on the particle bed at the bottom. This creates an artificially dense packing which is unlikely to happen in real experiments if particles are supplied from a hopper or vibrating feeder. On the other hand, when both the JKR and non-bonded models are used, particles can be attracted to each other and form clusters during free fall. This effect is particularly pronounced when the particles are initially close together with high initial packing fraction (i.e., 0.2). When the particles are sparsely generated, the particles have less chance to form clusters while falling especially those near the bottom, resulting in the arti-
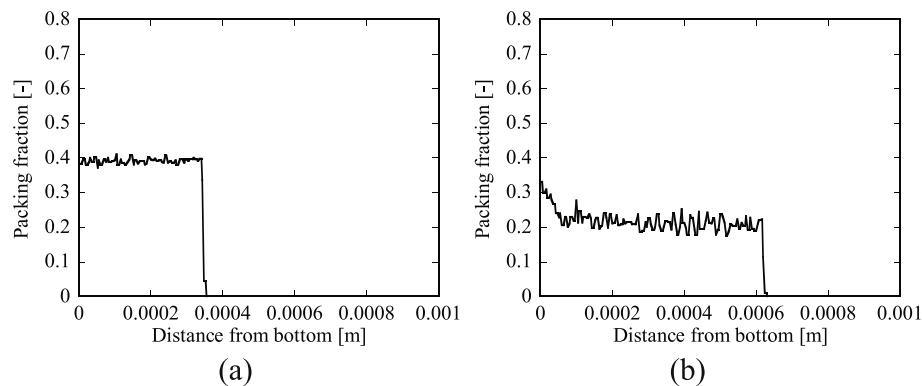

Fig. 7. Profiles of average packing fraction of the final beds in the vertical direction from the bottom; (a) JKR only model and (b) JKR + non-bonded model. The surface energy density used is 0.004 J/m², initial velocity is zero and initial packing fraction is 0.2.
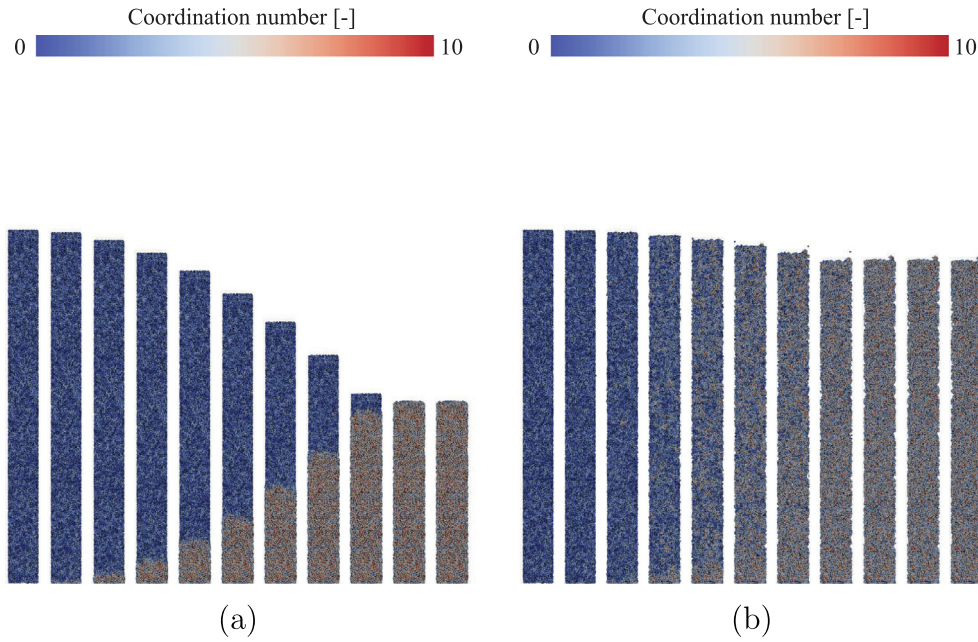
Fig. 8. Snapshots of particle bed; (a) JKR only model and (b) JKR + non-bonded model. Time range is 0 to 10 ms and interval is 1 ms for (a), and time range is 0 to 5 ms and interval is 0.5 ms for (b). The surface energy density used is 0.004 J/m², initial velocity is zero and initial packing fraction is 0.2.
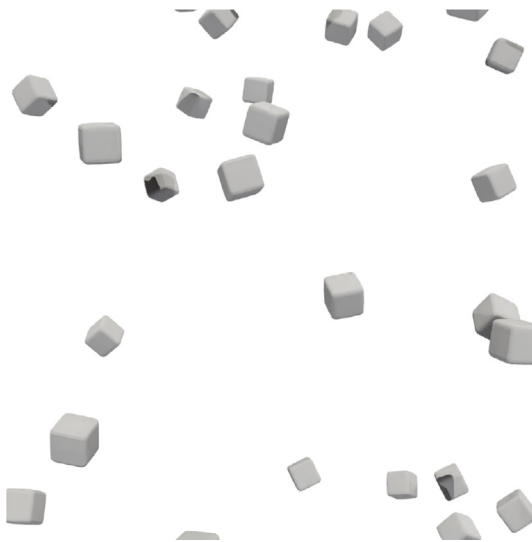

Fig. 9. Close-up view of particles generated with an initial packing fraction of 0.0034, ensuring no particle overlap.

ficial dense packing as mentioned above. These results suggest the importance of cluster formation during free fall for the packing of cohesive particles.

We then performed the same simulations of sparse particle distribution but with different initial vertical velocity, v_{init}, as:

$$v_{init,i} = -v_{ad} + c_{r,i} v_{vf} \tag{15}$$

where v_{ad} is the magnitude of average downward velocity, $c_{r,i}$ is the random number between -1 and 1 assigned to Particle i and v_{vf} is the magnitude of vertical velocity fluctuation. Figs. 12 and 13 show the profiles of packing fraction of the final beds from the bottom and sequential snapshots of the particle beds, respectively, with $v_{ad} = 0.5$ m/s. The vertical velocity fluctuation is 0 m/s for (a) and (b) and 0.5 m/s for (c) and (d). Interestingly, the packing fractions in Figs. 12a and 12b are very similar from the bottom to the middle

of the bed (up to 0.2 mm in height), implying the aforementioned artificially dense structure even with the non-bonded force. Due to the initial downward velocity, the time taken for the particles in this region to settle is much shorter, and they do not have sufficient chance to form clusters before landing. Once clusters start to form as can be seen at 40 ms onwards in Fig. 13b, however, the packing fraction decreases drastically as observed near the top of the bed in Fig. 12b. On the other hand, the packing fractions in Figs. 12c and 12d are much lower due to increased cluster formation induced by the random velocity fluctuations (as seen in Figs. 13c and 13d). It is noteworthy that the JKR only model can produce packing fraction below 0.4 although the profile is not flat in this specific case.

From the simulation results presented in Figs. 7–13, it is concluded that insufficient opportunities for particles interactions during free fall can lead to artificially high packing fraction, which is likely observed in the work of Parteli et al. [11]. This always occurs when the JKR only model is used with zero initial velocity fluctuation. However, similar packing structure can also be observed even when including the non-bonded model, suggesting that this force is not solely responsible for loose packing. Cluster formation may be induced by assigning initial vertical velocity fluctuations, and the packing fraction below 0.4 can be achieved by using the JKR only model. Therefore, vertical velocity fluctuations can be a good method to control the cluster formation. The challenge is that the resulting packing fraction profile may not be flat if particles are initially generated over the entire simulation domain (e.g., Figs. 10b, and 12c) which makes it difficult to define the meaningful average packing fraction of the bed. We employ a different particle insertion method to achieve flatter packing profile, as discussed in the next section.

4.2. Stream insertion of particles

In this section, we present simulation results using the stream insertion method. The simulation domain used is $(N \times 2a) \times (N \times 2a) \times (13333 \times 2a)$ where N ranges from 10 to 100, and the boundary conditions are the same as those used in Section 4.1. The particles are randomly generated with a fixed mass flow rate in a
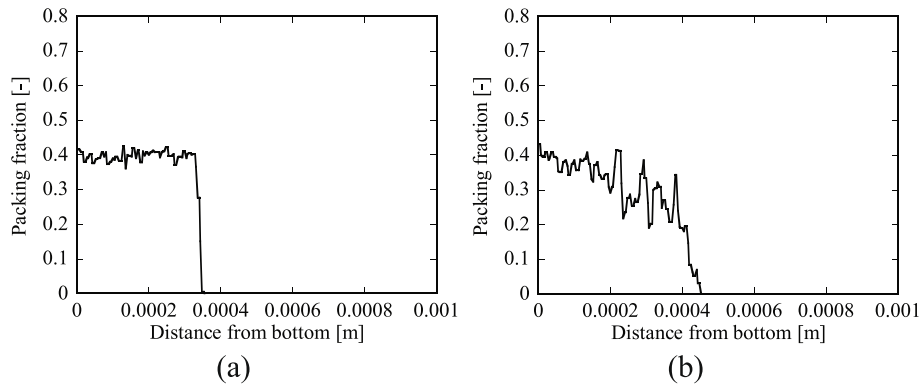
Fig. 10. Profiles of average packing fraction of the final beds in the vertical direction from the bottom; (a) JKR only model and (b) JKR + non-bonded model. The surface energy density used is 0.004 J/m², initial velocity is zero and initial packing fraction is 0.0034.
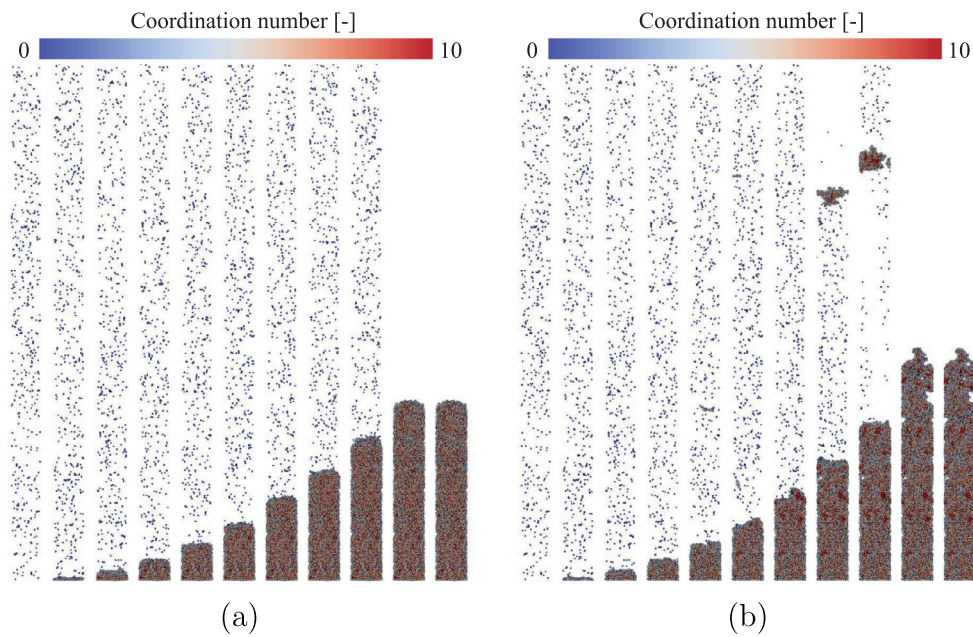

Fig. 11. Snapshots of particle bed; (a) JKR only model and (b) JKR + non-bonded model. Time range is 0 to 100 ms and interval is 10 ms. The surface energy density used is 0.004 J/m², initial velocity is zero and initial packing fraction is 0.0034.

factory region of the size $(N \times 2a) \times (N \times 2a) \times (267 \times 2a)$ whose centre is located at $(13133 \times 2a)$ in height. No overlap of particles is permitted at the generation.

4.2.1. At-once vs stream insertions

We first performed simulations to compare the at-once and stream insertion methods. The surface energy density used is 0.004 J/m² using the JKR + non-bonded model. N is 20 and the mass flow rate is 3.145×10^{-9} kg/s with zero initial velocity. These conditions are employed so that the packing fraction in the factory region becomes approximately 0.0034, which is used in the at-once insertion case in Figs. 10b and 11b.

Fig. 14 shows the profiles of average packing fraction of the final beds from the bottom obtained from the (a) at-once and (b) stream insertions. The plot in Fig. 10b is exactly the same as that in Fig. 14a, where the packing fraction declines with height. On the other hand, the profile of packing fraction in Fig. 14b is almost flat, which makes the evaluation of average packing fraction over the bed height easier.

Fig. 15 shows sequential snapshots of the particle beds. It can be seen that the particles form similar clusters throughout the simu-

lation with the stream insertion. The bed height in Fig. 15b increases linearly with time as opposed to the parabolic increase in Fig. 15a (which is the same as Fig. 11b). With the at-once insertion, the impact velocity of the particles landing on the bed varies with time since the duration when the particles are accelerated by gravity is dependent on the height at generation. The stream insertion, on the other hand, always generates particles in the same factory region and allows more consistent landing of the particles.

We have performed more simulations with different domain sizes, initial average velocities and velocity fluctuations as shown in the following sections, and confirmed that the stream insertion can consistently yield flat packing fraction profiles of the beds. It is concluded that the stream insertion is a more consistent and recommended method for studying the packing behaviour of fine and cohesive particles.

4.2.2. Effect of vertical velocity fluctuations

Next, we investigated the impact of vertical velocity fluctuation, v_{vf} in Eq. (15), on the cluster formation and the resultant packing fraction. The values of v_{vf} tested are between 0 and 1.25 m/s. The average downward velocity, v_{ad}, is fixed to 0.5 m/s. The horizontal
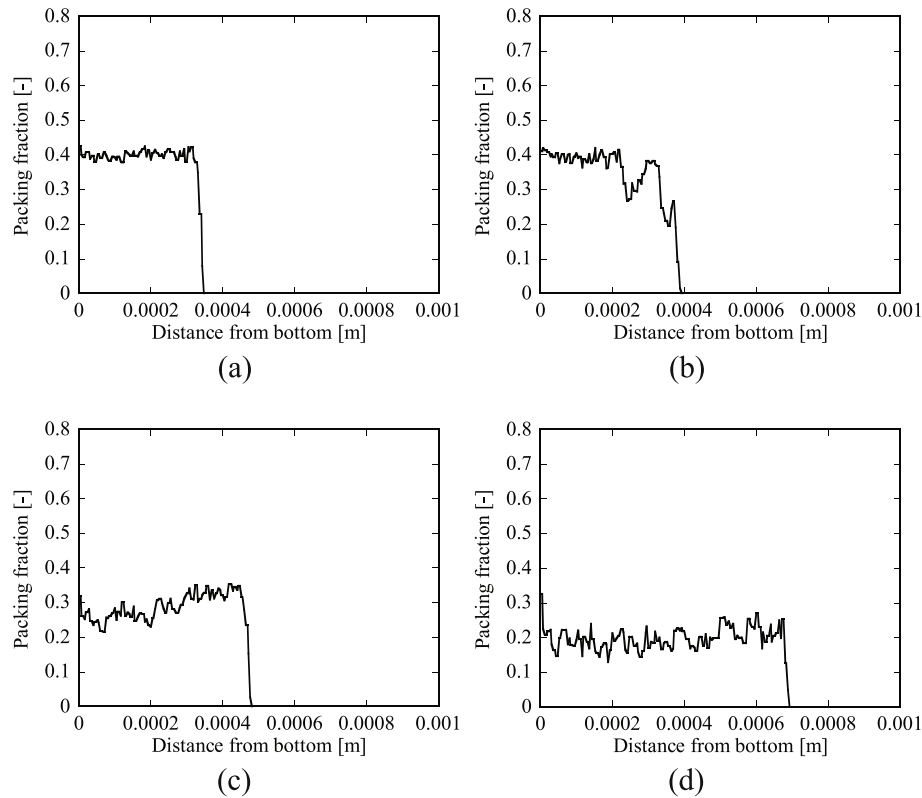
Fig. 12. Profiles of average packing fraction of the final beds in the vertical direction from the bottom; (a)&(c) JKR only model and (b)&(d) JKR + non-bonded model. The surface energy density used is 0.004 J/m², v_{ad} = 0.5 m/s and initial packing fraction is 0.0034. (a)&(b) v_{vf} = 0 m/s, and (c)&(d) v_{vf} = 0.5 m/s.

domain size is increased to $N = 100$ to ensure that the inter-cluster structures can be captured. The effect of domain size is discussed in the following section. The mass flow rate is fixed to 8.206×10^{-7} kg/s. The surface energy density used is 0.004 J/m², and the JKR + non-bonded model is employed.

Fig. 16 shows snapshots of clusters with different v_{vf} values at time 70 ms. It is clear that the cluster size increases with the vertical velocity fluctuation due to increased chances to collide and interact with other particles during free fall. Fig. 17 shows (a) the frequency of the coordination number of falling particles above the beds and (b) resultant average packing fraction of the final beds. The coordination number is analysed for the particles whose centre is located between 0.001 and 0.002 m in height. The top and bottom 10% of the final beds are excluded when computing the average packing fraction to eliminate the boundary effects. The peak of the coordination number increases with the vertical velocity fluctuation until v_{vf} = 0.25 m/s, after which the distribution becomes more or less similar especially those with v_{vf} = 0.5 and 1.25 m/s. The coordination number of the falling particles has a strong correlation with the average packing fraction in Fig. 17b: the average packing fraction also plateaus above v_{vf} = 0.25 m/s. It is concluded that the cluster formation can be controlled with the initial vertical velocity fluctuations until it reaches a critical value above which the cluster structure and the resultant packing fraction of the bed are not sensitive. We employ v_{vf} = 0.5 m/s in the following sections.

4.2.3. Effect of domain size

We then changed the horizontal domain size ranging from $N = 10$ to 100 to determine the critical domain size. The initial velocity is given by v_{ad} = 0.5 m/s and v_{vf} = 0.5 m/s as determined in Section 4.2.2. The mass flow rate is 8.206×10^{-7} kg/s when

$N = 100$, which is the same in Section 4.2.2, and scaled with the square of $N/100$. The surface energy density used is 0.004 J/m², and the JKR + non-bonded model is considered.

Fig. 18 shows (a) the profile of average packing fraction in the vertical direction and (b) the average packing fraction of the final beds as a function of domain size. When $N = 10$ the average packing fraction is notably high. This implies that the domain is too small and the inter-cluster structures and voids are not properly captured. As N increases to 20, the average packing fraction decreases, but the profile is still different from that of $N = 60$ or larger. It is noteworthy that in many simulations in the literature, the horizontal domain size used is between 10 and 20 times larger than the average particle diameter [9,11,12]. However, our simulations suggest that it might not be large enough if the particles can form clusters during free fall. We decided to use $N = 60$ in the simulations presented in the following section.

4.2.4. JKR only vs JKR + non-bonded models

In Section 4.1, we have presented that the packing fraction can be artificially high if particles are generated without initial overlap and individually land on the bed, which is particularly true with the JKR only model and is mitigated when the non-bonded force is included. However, the non-bonded force itself may not necessarily be responsible for loose packing of fine and cohesive particles. In this section, we present one of the key findings of this work; comparison between the JKR only and JKR + non-bonded models with equivalent surface energy densities as explained in Section 3. Three sets of simulations are carried out with (i) cohesionless, (ii) intermediately cohesive and (iii) highly cohesive cases. The equivalent surface energy densities from Fig. 5 are summarised in Table 3. The initial velocity is given by v_{ad} = 0.5 m/s and v_{vf} = 0.5 m/s, and the domain size is $N = 60$ as determined in Sec-
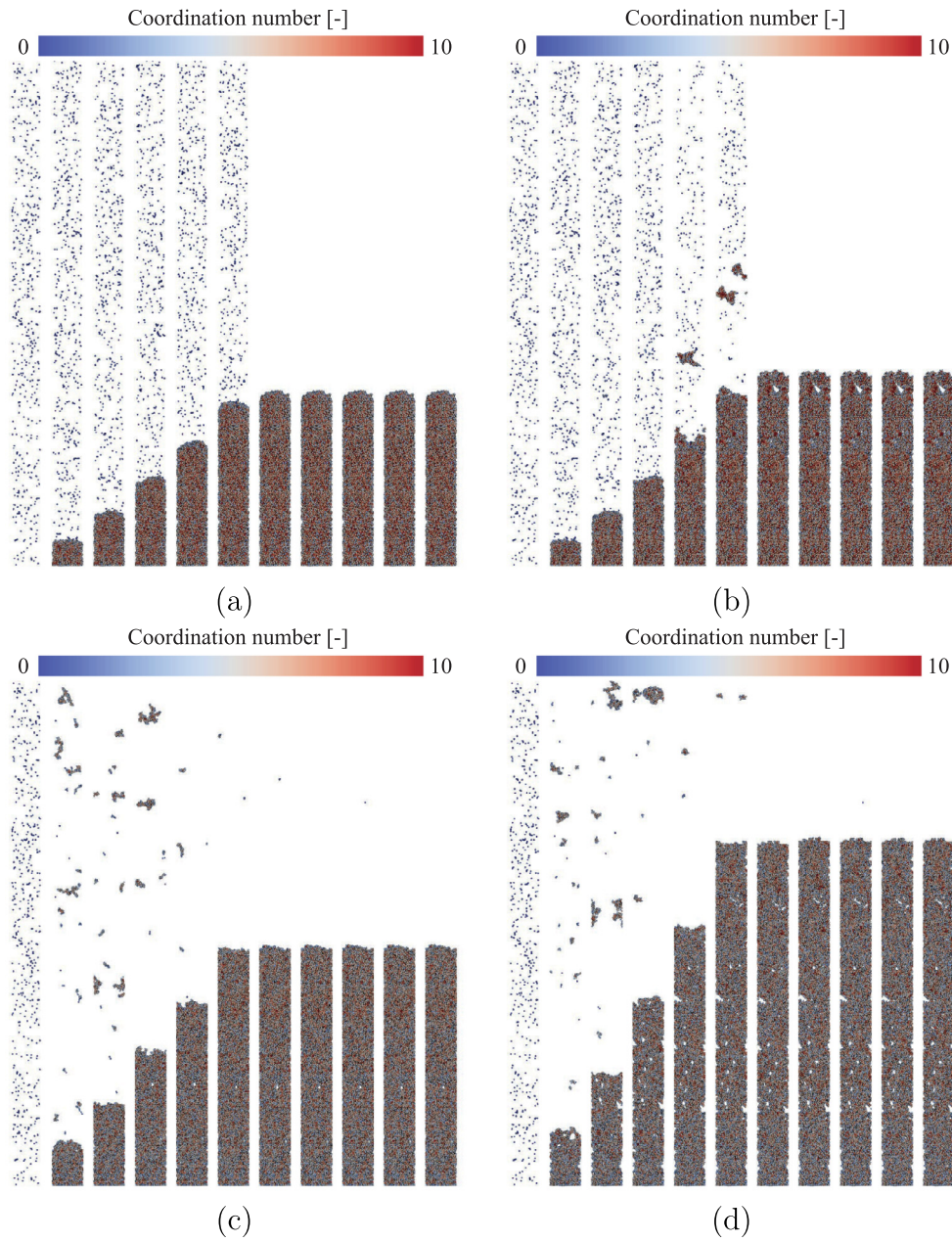
Fig. 13. Snapshots of particle bed; (a)&(c) JKR only model, and (b)&(d) JKR + non-bonded model. Time range is 0 to 100 ms and interval is 10 ms. The surface energy density used is 0.004 J/m², v_{ad} = 0.5 m/s and initial packing fraction is 0.0034. (a)&(b) v_{vf} = 0 m/s, and (c)&(d) v_{vf} = 0.5 m/s.
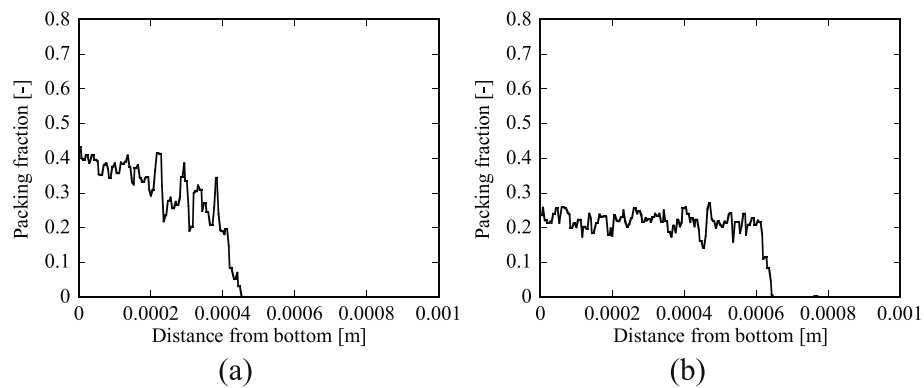

Fig. 14. Profiles of average packing fraction of the final beds in the vertical direction from the bottom; (a) at-once insertion and (b) stream insertion. The JKR + non-bonded model is used, the surface energy density is 0.004 J/m² and initial velocity is zero. The initial packing fraction is 0.0034.
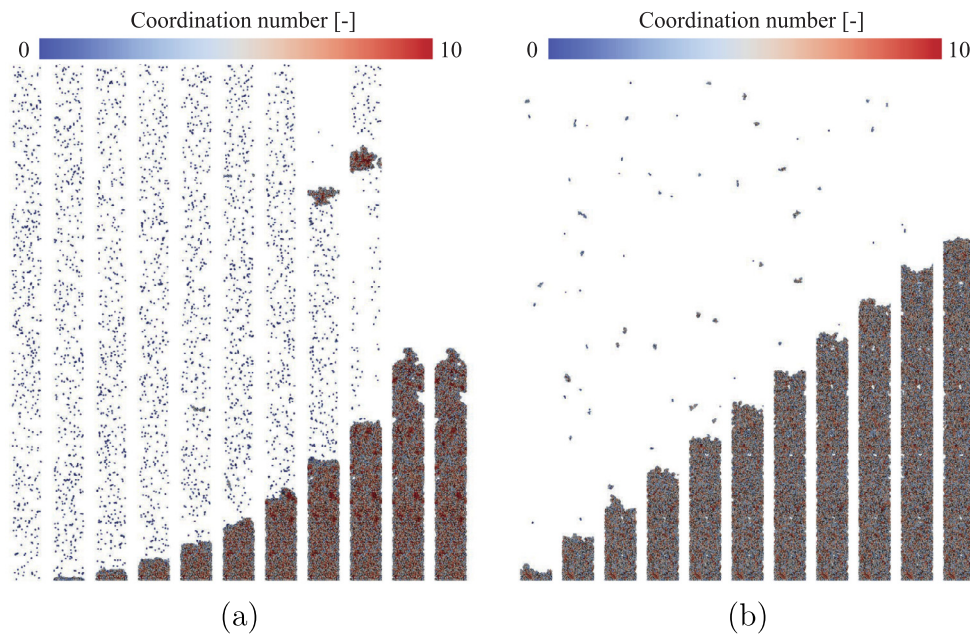
Fig. 15. Snapshots of particle bed; (a) at-once insertion and (b) stream insertion. Time range is 0 to 100 ms and interval is 10 ms for (a), and time range is 100 to 540 ms and interval is 44 ms for (b). The JKR + non-bonded model is used, the surface energy density is 0.004 J/m² and initial velocity is zero. The initial packing fraction is 0.0034.
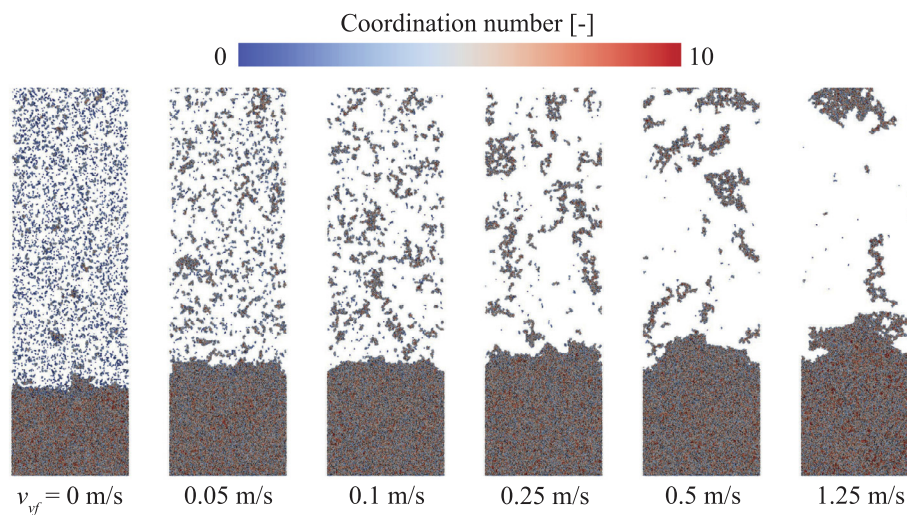

Fig. 16. Snapshots of clusters with different v_{vf} values at time 70 ms. The JKR + non-bonded model is used, and the surface energy density is 0.004 J/m². $N = 100$ and the mass flow rate is 8.206×10^{-7} kg/s.

tions 4.2.2 and 4.2.3, respectively. The mass flow rate is fixed to 2.954×10^{-7} kg/s.

Figs. 19 and 20 show the profile of average packing fraction and close-up views of internal particles of the final beds, respectively. When the surface energy density is zero, the particles are completely cohesionless and the results between the JKR only and JKR + non-bonded models are essentially identical. The average packing fraction can exceed 0.75, which is much higher than the random close packing of mono-sized spheres (approximately 0.64 [48]) as cubic particles can align their faces and form highly ordered arrangement. It is intuitive that the packing fraction decreases with increasing the surface energy density. In the intermediately cohesive case, the average packing fraction is approximately 0.45 in Fig. 19. In Fig. 20, it can be seen that the particles no longer align their faces although the structure is still homoge-

neous. Finally, in the highly cohesive cases, the particles can form very porous and heterogeneous structures and the average packing fraction reduces to about 0.2. Large voids between clusters can be observed in Fig. 20, which is qualitatively similar to those observed in Fig. 2. In all cases, the results obtained from the JKR only model are similar to those from the JKR + non-bonded model with equivalent surface energy densities.

Fig. 21 shows the frequency of particle coordination number in the final beds. The coordination number decreases with increasing the surface energy density, which is in line with the above observations. It is clear that the coordination numbers of the final beds are almost identical between the JKR only and JKR + non-bonded models in each case. This quantitatively proves that similar packing structure can be achieved regardless of the force model by using the equivalent surface energy densities that keep the same
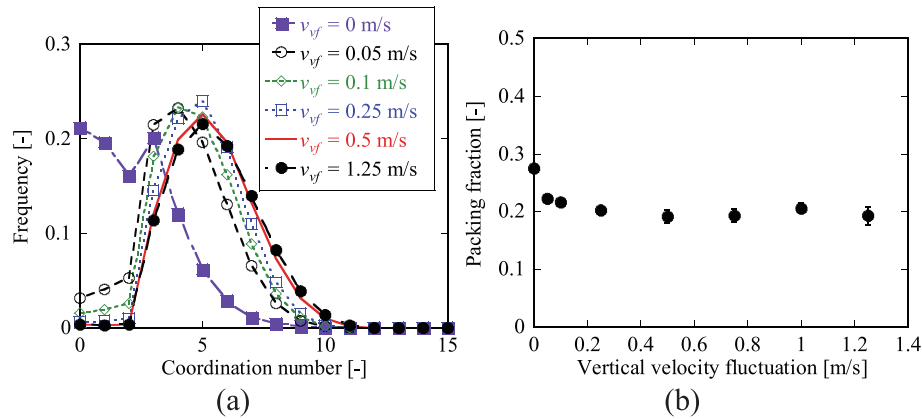
Fig. 17. Effect of vertical velocity fluctuation; (a) frequency of coordination number of falling particles and (b) average packing fraction of the final beds. The JKR + non-bonded model is used, and the surface energy density is 0.004 J/m². $N = 100$ and the mass flow rate is 8.206×10^{-7} kg/s.
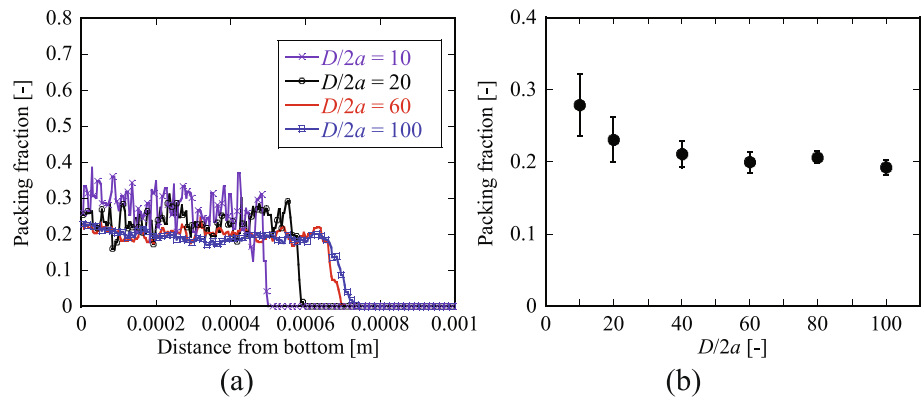

Fig. 18. Effect of horizontal domain size, $N = D/2a$; (a) profile of average packing fraction of the final beds in the vertical direction from the bottom and (b) average packing fraction of the final beds as a function of domain size. Both the JKR and non-bonded models are used, surface energy density is 0.004 J/m², $v_{ad} = 0.5$ m/s and $v_{vf} = 0.5$ m/s. The mass flow rate is $8.206 \times 10^{-7} \times (N/100)^2$ kg/s.

Table 3
Values of equivalent surface energy densities.

Cohesiveness	JKR only	JKR + non-bonded
Cohesionless	0 J/m²	0 J/m²
Intermediate	0.00105 J/m²	0.0004 J/m²
High	0.0105 J/m²	0.004 J/m²

total potential energy. The findings above can provide more flexibility in selecting the attraction force model for packing simulations. However, it is acknowledged that the non-bonded force may play an important role in some other contexts. The applicability of the present method to other processes will be explored in forthcoming publications.

5. Conclusions

In this work, various DEM simulations have been performed to investigate the impacts of (i) type of attraction forces and (ii) cluster formation during free fall on the packing behaviour of fine and cohesive particles. Two commonly used attraction force models, i.e., JKR only and JKR + non-bonded models are tested and compared. The key findings in each set of simulations are summarised below:
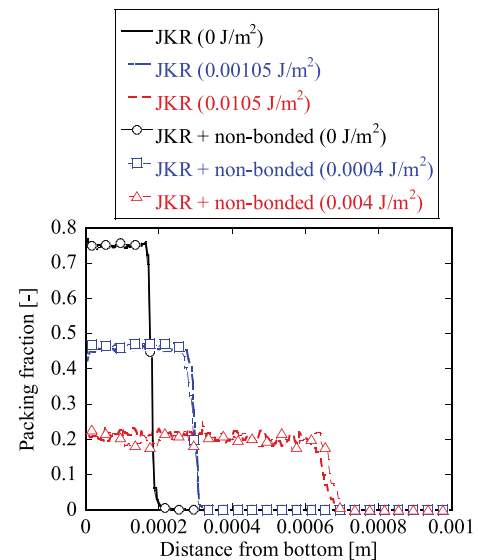

Fig. 19. Comparison between the JKR only and JKR + non-bonded models; profile of average packing fraction of the final beds in the vertical direction from the bottom. $v_{ad} = 0.5$ m/s and $v_{vf} = 0.5$ m/s. $N = 60$ and the mass flow rate is 2.954×10^{-7} kg/s.
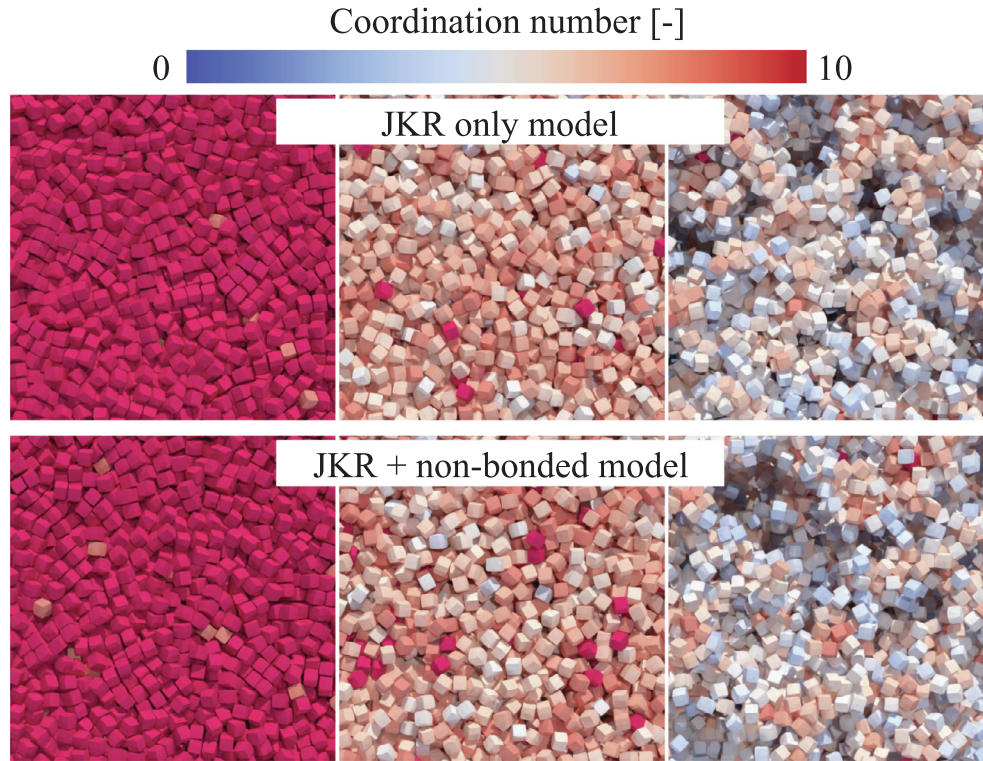
Fig. 20. Close-up views of internal particles in the final beds; (left) cohesionless, (middle) intermediately cohesive and (right) highly cohesive cases. $v_{ad} = 0.5$ m/s and $v_{vf} = 0.5$ m/s. $N = 60$ and the mass flow rate is 2.954×10^{-7} kg/s.
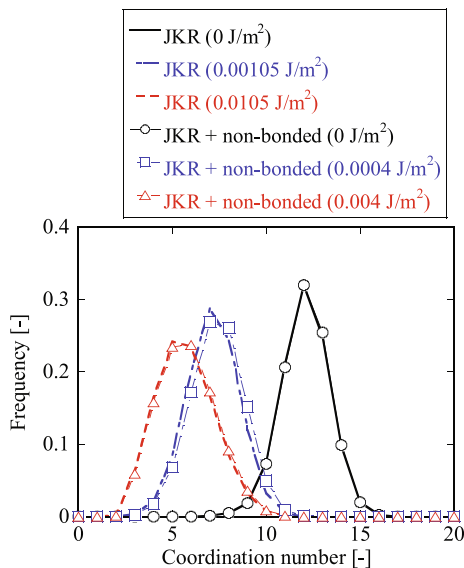

Fig. 21. Comparison between the JKR only and JKR + non-bonded models; frequency of particle coordination number in the final beds. $v_{ad} = 0.5$ m/s and $v_{vf} = 0.5$ m/s. $N = 60$ and the mass flow rate is 2.954×10^{-7} kg/s.

- Artificially dense packing is observed if particles are generated without initial overlap and individually land on the bed. This always happens with the JKR only model if no initial velocity is given to the particles. This is likely the reason of the high packing fraction reported by Parteli et al. [11].

- Introduction of non-bonded force may mitigate the artificially high packing. However, it is not necessarily solely responsible for loose packing of cohesive particles.
- Cluster formation of free falling particles can be induced by assigning initial vertical velocity fluctuations. The coordination numbers of falling particles do not change above the critical fluctuation velocity (0.5 m/s in this study).
- Stream insertion creates consistently flat packing fraction profiles compared to at-once insertion.
- The simulation domain size should be sufficiently large to capture the inter-cluster structures. The packing fraction may be overestimated with typical horizontal domain sizes used in the literature (10 to 20 times the particle size).
- Quantitatively similar packing structure can be achieved with different attraction force models as long as (i) the surface energy density is adjusted by approximately 2.6 times to match the total potential energy between a pair of particles and (ii) the initial vertical velocity fluctuations are assigned to form particle clusters during free fall at the same time.

Declaration of Competing Interest

The authors declare that they have no known competing financial interests or personal relationships that could have appeared to influence the work reported in this paper.

Acknowledgements

ogy in Kyushu University, and the supercomputer of ACCMS in Kyoto University.

References

[1] G.D. Scott, Packing of spheres: packing of equal spheres, Nature 188 (1960) 908–909.

[2] Z. Zhang, L. Liu, Y. Yuan, A. Yu, A simulation study of the effects of dynamic variables on the packing of spheres, Powder Technol. 116 (2001) 23–32.

[3] M. Gan, N. Gopinathan, X. Jia, R.A. Williams, Predicting packing characteristics of particles of arbitrary shapes, KONA Powder and Particle Journal 22 (2004) 82–93.

[4] H.P. Zhu, Z.Y. Zhou, R.Y. Yang, A.B. Yu, Discrete particle simulation of particulate systems: A review of major applications and findings, Chem. Eng. Sci. 63 (2008) 5728–5770.

[5] J. Visser, Van der waals and other cohesive forces affecting powder fluidization, Powder Technol. 58 (1989) 1–10.

[6] A. Yu, J. Bridgwater, A. Burbidge, On the modelling of the packing of fine particles, Powder Technol. 92 (1997) 185–194.

[7] G. Roquier, Evaluation of three packing density models on reference particle-size distributions, Granular Matter 26 (2024) 7.

[8] P.A. Cundall, O.D.L. Strack, A discrete numerical model for granular assemblies, Géotechnique 29 (1979) 47–65.

[9] R.Y. Yang, R.P. Zou, A.B. Yu, Computer simulation of the packing of fine particles, Phys. Rev. E 62 (2000) 3900–3908.

[10] S. Yang, K. Dong, R. Zou, A. Yu, J. Guo, Packing of fine particles in an electrical field, Granular Matter 15 (2013) 467–476.

[11] E.J. Parteli, J. Schmidt, C. Blümel, K.E. Wirth, W. Peukert, T. Pöschel, Attractive particle interaction forces and packing density of fine glass powders, Scient. Rep. 4 (2014) 1–7.

[12] W. Liu, S. Chen, S. Li, Random loose packings of polydisperse adhesive microparticles with gaussian size distribution, Powder Technol. 357 (2019) 64–73.

[13] J. Gan, A. Yu, Dem study on the packing density and randomness for packing of ellipsoids, Powder Technol. 361 (2020) 424–434.

[14] A.P. Santos, D.S. Bolintineanu, G.S. Grest, J.B. Lechman, S.J. Plimpton, I. Srivastava, L.E. Silbert, Granular packings with sliding, rolling, and twisting friction, Phys. Rev. E 102 (2020) 032903.

[15] Y. He, A. Hassanpour, M.A. Behjani, A.E. Bayly, A novel stiffness scaling methodology for discrete element modelling of cohesive fine powders, Appl. Math. Model. 90 (2021) 817–844.

[16] X.L. Deng, R.N. Davé, Dynamic simulation of particle packing influenced by size, aspect ratio and surface energy, Granular Matter 15 (2013) 401–415.

[17] R. Tayeb, X. Dou, Y. Mao, Y. Zhang, Analysis of cohesive microsized particle packing structure using history-dependent contact models, J. Manuf. Sci. Eng. 138 (2016) 041005.

[18] H.S. Elmsahli, I.C. Sinka, A discrete element study of the effect of particle shape on packing density of fine and cohesive powders, Computational Particle Mechanics 8 (2021) 183–200.

[19] K.Z.Y. Yen, T.K. Chaki, A dynamic simulation of particle rearrangement in powder packings with realistic interactions, J. Appl. Phys. 71 (1992) 3164–3173.

[20] K.J. Dong, R.Y. Yang, R.P. Zou, A.B. Yu, Settling of particles in liquids: Effects of material properties, AIChE J. 58 (2012) 1409–1421.

[21] K.L. Johnson, K. Kendal, A.D. Roberts, Surface energy and the contact of elastic solids, Proceedings of the Royal Society of London. A. Mathematical and Physical Sciences 324 (1971) 301–313.

[22] H. Hamaker, The london–van der waals attraction between spherical particles, Physica 4 (1937) 1058–1072.

[23] M.E. Möbius, Clustering instability in a freely falling granular jet, Phys. Rev. E 74 (2006) 051304.

[24] J.R. Royer, D.J. Evans, L. Oyarte, Q. Guo, E. Kapit, M.E. Möbius, S.R. Waitukaitis, H.M. Jaeger, High-speed tracking of rupture and clustering in freely falling granular streams, Nature 459 (2009) 1110–1113.

[25] Y. Nagaashi, T. Omura, M. Kiuchi, A.M. Nakamura, K. Wada, S. Hasegawa, Laboratory experiments on agglomeration of particles in a granular stream, Progress in Earth and Planetary Science 5 (2018) 52.

[26] Y. Nagaashi, A.M. Nakamura, S. Hasegawa, K. Wada, Packing fraction of clusters formed in free-falling granular streams based on flash x-ray radiography, Phys. Rev. E 103 (2021) 032903.

[27] S.R. Waitukaitis, H.F. Grütjen, J.R. Royer, H.M. Jaeger, Droplet and cluster formation in freely falling granular streams, Phys. Rev. E 83 (2011) 051302.

[28] S. Ulrich, A. Zippelius, Stability of freely falling granular streams, Phys. Rev. Lett. 109 (2012) 166001.

[29] P. Liu, C.M. Hrenya, Cluster-induced deagglomeration in dilute gravity-driven gas-solid flows of cohesive grains, Phys. Rev. Lett. 121 (2018) 238001.

[30] J. Hærvig, U. Kleinhans, C. Wieland, H. Spliethoff, A. Jensen, K. Sørensen, T. Condra, On the adhesive jkr contact and rolling models for reduced particle stiffness discrete element simulations, Powder Technol. 319 (2017) 472–482.

[31] M. Macaulay, P. Rognon, Viscosity of cohesive granular flows, Soft Matter 17 (2021) 165–173.

[32] C. Kloss, C. Goniva, A. Hager, S. Amberger, S. Pirker, Models, algorithms and validation for opensource dem and cfd-dem, Progress in Computational Fluid Dynamics 12 (2012) 140–152.

[33] K. Washino, E.L. Chan, T. Tsujimoto, T. Tsuji, T. Tanaka, Development of resolved cfd–dem coupling model for three-phase flows with non-spherical particles, Chem. Eng. Sci. 267 (2023) 118335.

[34] K. Washino, E.L. Chan, Y. Nishida, T. Tsuji, Coarse grained dem simulation of non-spherical and poly-dispersed particles using scaled-up particle (sup) model, Powder Technol. 426 (2023) 118676.

[35] Barr, Superquadrics and angle-preserving transformations, IEEE Computer Graphics and Applications 1 (1981) 11–23.

[36] A. Podlozhnyuk, S. Pirker, C. Kloss, Efficient implementation of superquadric particles in discrete element method within an open-source framework, Computational Particle Mechanics 4 (2017) 101–118.

[37] G. Pozzetti, B. Peters, A multiscale dem-vof method for the simulation of three-phase flows, Int. J. Multiph. Flow 99 (2018) 186–204.

[38] Y. Tsuji, T. Tanaka, T. Ishida, Lagrangian numerical simulation of plug flow of cohesionless particles in a horizontal pipe, Powder Technol. 71 (1992) 239–250.

[39] C. Thornton, Interparticle sliding in the presence of adhesion, J. Phys. D: Appl. Phys. 24 (1991) 1942–1946.

[40] J.S. Marshall, Discrete-element modeling of particulate aerosol flows, J. Comput. Phys. 228 (2009) 1541–1561.

[41] M. Pasha, C. Hare, A. Hassanpour, M. Ghadiri, Analysis of ball indentation on cohesive powder beds using distinct element modelling, Powder Technol. 233 (2013) 80–90.

[42] K.O. Braschke, J. Zoller, F. Freese, A. Dittler, U. Janoske, Fast adhesion calculation for collisions between arbitrarily shaped particles and a wall, Powder Technol. 405 (2022) 117494.

[43] J. Lee, E. Nakouzi, J. Heo, B.A. Legg, G.K. Schenter, D. Li, C. Park, H. Ma, J. Chun, Effects of particle shape and surface roughness on van der waals interactions and coupling to dynamics in nanocrystals, J. Colloid Interface Sci. 652 (2023) 1974–1983.

[44] K. Washino, E.L. Chan, T. Tanaka, Dem with attraction forces using reduced particle stiffness, Powder Technol. 325 (2018) 202–208.

[45] K. Washino, S. Nakae, R. Yamagami, E.L. Chan, T. Tsuji, T. Tanaka, Scaling of attraction force and rolling resistance in dem with reduced particle stiffness, Chem. Eng. Res. Des. 203 (2024) 501–519.

[46] R.Y. Yang, R.P. Zou, A.B. Yu, Effect of material properties on the packing of fine particles, J. Appl. Phys. 94 (2003) 3025–3034.

[47] R.C. Hidalgo, D. Kadau, T. Kanzaki, H.J. Herrmann, Granular packings of cohesive elongated particles, Granular Matter 14 (2012) 191–196.

[48] W. Liu, S. Li, A. Baule, H.A. Makse, Adhesive loose packings of small dry particles, Soft Matter 11 (2015) 6492–6498.